

Communication

# Boosting Water Oxidation Activity via Carbon–Nitrogen Vacancies in NiFe Prussian Blue Analogue Electrocatalysts

Meng Zhang, Wenjie Wu, Zhen Wang, Gang Xie \* and Xiaohui Guo \*

Key Laboratory of Synthetic and Natural Functional Molecule of the Ministry of Education, College of Chemistry & Materials Science, Shaanxi Key Laboratory for Carbon Neutral Technology, Northwest University, Xi'an 710127, China

\* Correspondence: gangxie@nwu.edu.cn (G.X.); guoxh2009@nwu.edu.cn (X.G.)

**Abstract:** The development of electrocatalysts for oxygen evolution reactions (OERs) is of great significance for hydrogen production. Defect engineering is an effective strategy to improve the OER performance of electrocatalyst by regulating the local electronic and atomic structures of electrocatalysts. Here, we successfully synthesized defective Prussian blue analogues (PBAs) with rich CN vacancies (D-NiFe PBA) as efficient OER electrocatalysts. The optimized D-NiFe PBA exhibited an overpotential of 280 mV at 10 mA cm<sup>-2</sup> and a superior stability for over 100 h in KOH electrolytes. The formation of CN vacancies in the NiFe PBA could effectively inhibit the loss of Fe active sites, promote the reconstruction of the NiFe oxygen (hydroxide) active layer in the OER process, and further improve the electrocatalytic activity and stability of the V<sub>CN</sub>-NiFe PBA. This work presents a feasible approach for the wide application of vacancy defects in PBA electrocatalysts.

**Keywords:** Prussian blue analogues; vacancy; OER; activity; stability



**Citation:** Zhang, M.; Wu, W.; Wang, Z.; Xie, G.; Guo, X. Boosting Water Oxidation Activity via Carbon–Nitrogen Vacancies in NiFe Prussian Blue Analogue Electrocatalysts. *Colloids Interfaces* **2023**, *7*, 14. <https://doi.org/10.3390/colloids7010014>

Academic Editors: Abhijit Dan and Aruna Dhathathreyan

Received: 16 January 2023

Revised: 5 February 2023

Accepted: 8 February 2023

Published: 10 February 2023



**Copyright:** © 2023 by the authors. Licensee MDPI, Basel, Switzerland. This article is an open access article distributed under the terms and conditions of the Creative Commons Attribution (CC BY) license (<https://creativecommons.org/licenses/by/4.0/>).

## 1. Introduction

With the worsening of the global climate, carbon neutrality is being considered as a national strategy by many countries. Hydrogen production from water electrolysis is an important technique for future hydrogen energy production to replace transitional fossil energy [1]. However, hydrogen production performance mainly depends on the performance of the half oxygen evolution reaction (OER) because the OER suffers from a sluggish four-electron process. Since electrocatalysts can effectively reduce the OER energy barriers and accelerate the reaction kinetics, developing efficient electrocatalysts for the OER has aroused wide research interest [2,3]. Currently, several noble metal oxides, such as RuO<sub>2</sub> and IrO<sub>2</sub>, are the most widely used OER electrocatalysts. However, their rarity, high cost, and unstable features limit their large-scale application. Therefore, developing efficient and low-cost OER electrocatalysts has become extremely important for industrial hydrogen production [4].

Prussian blue analogues (PBAs) have been widely applied as electrocatalyst for water oxidation in recent years owing to their defined structure, low cost, easy modification, and stability. Generally, the formula of PBAs is A<sub>x</sub>M[Fe(CN)<sub>6</sub>]<sub>y</sub>·mH<sub>2</sub>O (0 ≤ x ≤ 2, y < 1), where A represents an alkali metal and M represents a transition metal [5,6]. In PBA nanomaterials, nitrogen-ligated M cations and carbon-ligated Fe sites are bridged by cyanide (CN) groups to form an open framework [7]. Although PBA electrocatalysts have been reported previously in the literature, the inherent poor conductivity of PBAs still limits the further improvement of their OER efficiency [8–10]. Therefore, continuously improving the electrocatalytic performance of PBAs is still challenging.

Defect engineering is an effective strategy to enhance the OER performance of electrocatalysts, which can regulate the local electronic and atomic structures of electrocatalysts. Recently, Yu et al. reported that nitrogen plasma treatment can overcome the energy barrier and break the bond between the transition metal and CN groups, resulting in unusual

CN vacancies that can facilitate electron transfer and improve the OER performance [11]. Jiang et al. demonstrated that CN vacancies could effectively regulate the local electronic structure and coordination environment of Ni–Fe sites. The obtained PBA with abundant CN vacancies exhibited an impressive OER activity (267 mV at 20 mA cm<sup>-2</sup>) [5,12–15]. Although several methods for creating CN vacancy defects in PBAs have been reported, these methods suffer from high costs, large energy consumptions, and expensive instruments. Therefore, exploiting simple and efficient methods with low energy consumption in order to construct defective PBAs with rich CN vacancies is of great significance.

Several studies have demonstrated that the NaBH<sub>4</sub> reduction method is a mature manner for the generation of defects in various materials. Xiang et al. prepared two-dimensional ZnCo<sub>2</sub>O<sub>4</sub> nanosheets with abundant oxygen vacancies based on the reduction of NaBH<sub>4</sub> [16]. Yan et al. also employed NaBH<sub>4</sub> as a reducing agent to synthesize CoFe<sub>2</sub>O<sub>4</sub> nanosheets containing rich oxygen vacancies [17]. Wang et al. successfully prepared Co<sub>3</sub>O<sub>4</sub> via the NaBH<sub>4</sub> reduction method, which exhibited a better electrocatalytic activity in the OER compared with P-Co<sub>3</sub>O<sub>4</sub> NSA [18]. All the above studies verified that the NaBH<sub>4</sub> reduction method has been used well to produce defects in various electrocatalysts. To the best of our knowledge, to date, constructing D-PBAs with rich CN vacancies using NaBH<sub>4</sub> as a reduction agent has not been reported.

Herein, CN vacancies ( $V_{\text{CN}}$ ) were successfully generated in NiFe PBAs via the NaBH<sub>4</sub> reduction strategy. A concentration of  $V_{\text{CN}}$  in the defective NiFe PBAs (D-NiFe PBA) as high as 24% was reached. The experimental results showed that the overpotential of the D-NiFe PBA (280 mV at 10 mA cm<sup>-2</sup>) was substantially reduced compared with that of the NiFe PBA (450 mV at 10 mA cm<sup>-2</sup>). Moreover, the D-NiFe PBA was electrocatalytically stable for over 100 h in alkaline electrolytes. The reported approach paves the way for the development of high-performance electrocatalysts for industrial hydrogen production.

## 2. Materials and Methods

### 2.1. Materials Reagents and Synthesis Conditions

In this process, 1.95 mL (1 M) NiCl<sub>2</sub> and 1.05 mL (1 M) K<sub>3</sub>Fe(CN)<sub>6</sub> aqueous solutions were ultrasonically mixed together and kept static at room temperature. After four hours, NiFe PBA was obtained. Subsequently, a 0.2 g mL<sup>-1</sup> NaBH<sub>4</sub> aqueous solution was added to the above mixture under vigorous stirring, and was then kept static for 24 h. Finally, the black D-NiFe PBA was separated by centrifugation at 10,000 rpm, completely washed with water and ethanol, and then dried at 60 °C for 24 h.

### 2.2. Physical Characterization

Powder X-ray diffraction (PXRD) patterns were obtained on a Bruker D8 Advance X-ray Diffractometer by using Cu–K $\alpha$  radiation ( $\lambda = 0.15418$  nm) with a  $2\theta$  range from 10° to 80° at a scan speed of 0.1° s<sup>-1</sup>. Scanning electron microscopy (SEM) images were obtained with a Hitachi SU8010 electron microscope (Hitachi, Tokyo, Japan) with an accelerating voltage of 3 kV. A Talos-F200X (TEM) (Thermo Scientific, Waltham, MA, USA) transmission electron microscope was used to acquire the TEM, HRTEM, and EDX mapping images at 200 kV. X-ray photoelectron spectroscopy (XPS) was carried out by using a PHI5000 Versa Probe III XPS spectrometer (ULVAC-PHI, Tokyo, Japan) equipped with an achromatic Al–K $\alpha$  (1486.6 eV) X-ray source. The binding energy scale of the spectrometer was calibrated by using the position of the C1s peak at 284.6 eV. A Bruker VECTOR-22 FTIR spectrometer was used to record the Fourier transform infrared (FT–IR) spectra ranging from 4000 to 400 cm<sup>-1</sup>. Elemental analysis (EA) and inductively coupled plasma mass spectrometry (ICP–MS) measurements (Agilent 7500, Tokyo, Japan) were conducted to analyze the samples. EPR spectra were obtained from a JEOL JES-FA300 EPR spectrometer (Bruker Instruments, Bremen, Germany).

### 2.3. Electrochemical Characterization

All electrochemical measurements were carried out on a CHI660E electrochemical workstation (Chen Hua, Shanghai, China) with a three-electrode system in KOH electrolyte (1 M). A platinum (Pt)-foil electrode and a saturated-glycerol electrode were used as the counter and reference electrodes, respectively, wherein, a glass carbon RDE (4 mm in diameter; area: 0.1256 cm<sup>2</sup>) was selected as catalyst substrate. For the preparation of the working electrodes, 5 mg of catalyst and 1 mg of conductive carbon black were added into 1 mL of an aqueous solution containing 20 μL of 5 wt% Nafion and ultrasonicated for 30 min to obtain a uniformly dispersed black suspension. Then, 10 mL of the suspension was dropped onto the electrode surface and dried at room temperature. The calculated active substance loaded on glass carbon RDE was about 0.39 mg cm<sup>-2</sup>. The potentials in this work were converted to RHE, yielding the equation  $E_{\text{RHE}} = 0.098 \text{ V} + 0.059 \times \text{pH} + E_{\text{Hg}/\text{HgO}}$  (RHE). A commercial IrO<sub>2</sub> catalyst obtained from Aladdin was used for comparison. All polarization curves were gained from linear sweep voltammetry (LSV) at a scan rate of 1 mV s<sup>-1</sup> until stability was achieved, which for the OER was between 1.2 and 1.8 V (vs. RHE). A linear trend was observed through the current density (vs. RHE) versus the scan rate. The electrochemical impedance spectrum (EIS) of the D-NiFe PBA was tested at a potential of 1.524 V vs. RHE (amplitude 5 mV) in 1 M KOH solution over a frequency range from 100 mHz to 100 kHz. The electrochemically active surface area (ECSA) was evaluated with cyclic voltammogram (CV) measurements at non-faradaic overpotentials. The CV measurements were performed at various scan rates (20, 40, 60, 80, and 100 mV s<sup>-1</sup>) in the range of 0.924–1.024 versus RHE. The double-layer capacitance (C<sub>dl</sub>) was tested by plotting  $\Delta j = (j_+ - j_-)/2$  at 0.974 V vs. RHE against the scan rate. The ECSA was evaluated by the following equation: ECSA = C<sub>dl</sub>/0.04 mF cm<sup>-2</sup> per cm<sup>2</sup>. For long-term stability testing, the catalyst was dropped onto carbon paper (area: 1 × 1 cm<sup>2</sup>; mass loading: 0.39 mg cm<sup>-2</sup>).

### 3. Results and Discussion

The schematic diagram for the synthesis of the D-NiFe PBA is shown in Figure 1. First, the NiFe PBA sample was prepared by the co-precipitation method according to a previous study [3]. Then, the D-NiFe PBA was obtained via the reduction of NaBH<sub>4</sub>. The NaBH<sub>4</sub> could break the Fe-C and Ni-N bonds in the Fe-CN-Ni unit of the NiFe PBA and generate CN<sup>-</sup> diffusion away from the NiFe PBA lattices, resulting in the formation of V<sub>CN</sub> in the NiFe PBA. The PXRD patterns of the prepared NiFe PBA are shown in Figure 2a. The NiFe PBA corresponded to a Ni<sub>2</sub>Fe(CN)<sub>6</sub> · xH<sub>2</sub>O crystal structure (JCPDS No.14-0291), and no additional peaks of impurities were detected, indicating the high purity of the NiFe PBA. In addition, the PXRD spectrum of the D-NiFe PBA was basically consistent with that of the NiFe PBA, implying that the crystal structure of the NiFe PBA did not alter remarkably after the NaBH<sub>4</sub> reduction [11]. The surface morphology of the D-NiFe PBA was examined via SEM and TEM, as shown in Figure 2b,c. The D-NiFe-PBA presented a two-dimensional nanosheet, which is beneficial for enhancing the number of active sites exposed on the surfaces [19]. The SEM image indicates that the NiFe PBA was formed of small nanoparticles that were interconnected with each other to form 3D nanonetworks, as shown in Figure S1a. In addition, Figure S1b provides the elemental mapping results. Clearly, Ni, Fe, C, and N elements were well-distributed throughout the whole sample. The HRTEM image of the D-NiFe PBA is shown in Figure 2d. The lattice spacing of 0.505 nm was assigned to the (200) plane of the Ni<sub>2</sub>Fe(CN)<sub>6</sub> · xH<sub>2</sub>O [3]. In addition, the EDX result shown in Figure 2e showed a homogeneous distribution of Ni, Fe, C, and N elements, and all the elements in the D-NiFe PBA were evenly distributed with no significant C and N discoloration.

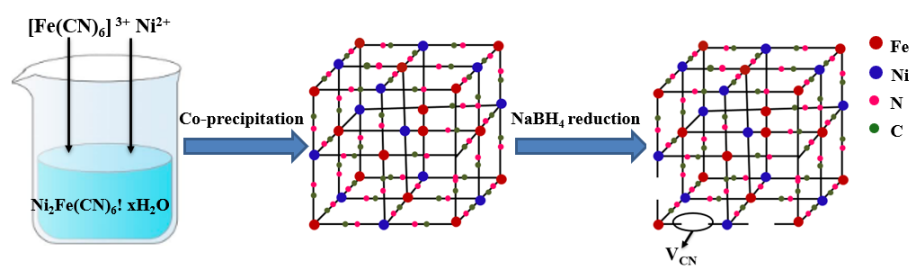


**Figure 1.** The schematic illustration of the synthetic process of D-NiFe PBA.

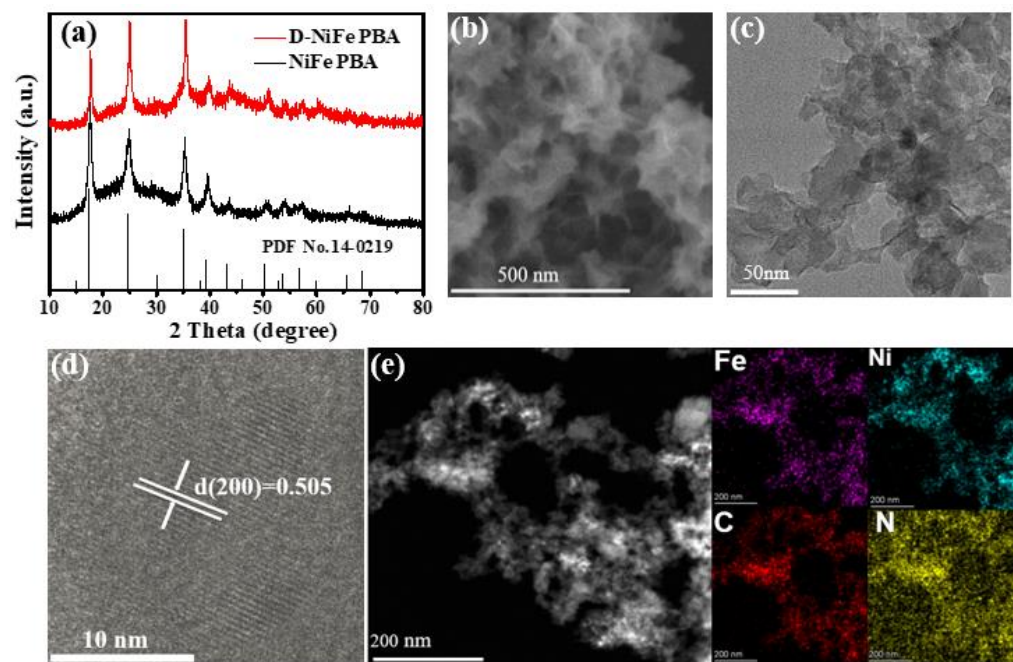


**Figure 2.** (a) PXRD spectra of NiFe PBA and D-NiFe PBA. (b) SEM images of D-NiFe PBA. (c) TEM images of D-NiFe PBA. (d) HRTEM images of D-NiFe PBA. (e) EDX element mapping for D-NiFe PBA.

Raman spectra, FTIR spectra, ICP-MS, and EA characterizations were obtained to evaluate the structural changes of the NiFe PBA before and after the  $\text{NaBH}_4$  reduction. As depicted in Figure 3a, the Raman spectrum of the NiFe PBA exhibited two prominent peaks concentrated at  $2095$  and  $2142\text{ cm}^{-1}$ , both corresponding to the CN vibrations of  $\text{Fe}^{\text{II}}\text{-CN-Ni}^{\text{II}}$  and  $\text{Fe}^{\text{II}}\text{-CN-Ni}^{\text{III}}$  [20–22], respectively. By contrast, the Raman peak of the D-NiFe PBA was negatively shifted, which indicated an increase in  $V_{\text{CN}}$  in the D-NiFe PBA [23]. Figure 3b shows the FT-IR spectra of the NiFe PBA and D-NiFe PBA, where the band at  $2081$  and  $1632\text{ cm}^{-1}$  corresponded to the characteristics of the CN group in the PBA [12,24,25]. The spectra of the D-NiFe PBA were almost identical to those of the NiFe PBA, and slight peak decreases in the D-NiFe PBA were observed, which suggested the presence of  $V_{\text{CN}}$  [23]. Furthermore, according to the ICP-MS result shown in Table S1, the content of  $V_{\text{CN}}$  in the NiFe PBA and the D-NiFe PBA was calculated according to ICP-MS (measuring Fe and Ni) and EA (measuring C and N). The ICP-MS and EA results all proved that the volumetric atomic ratios of Fe/Ni and C/N of the PBA remained constant after the  $\text{NaBH}_4$  reduction, but the atomic rates of N/Ni and C/Fe decreased with time, and the results indicated that only  $V_{\text{CN}}$  and no other vacancy defects were present in the NiFe PBA. After calculation, the D-NiFe PBA had a  $V_{\text{CN}}$  content of approximately 24%.

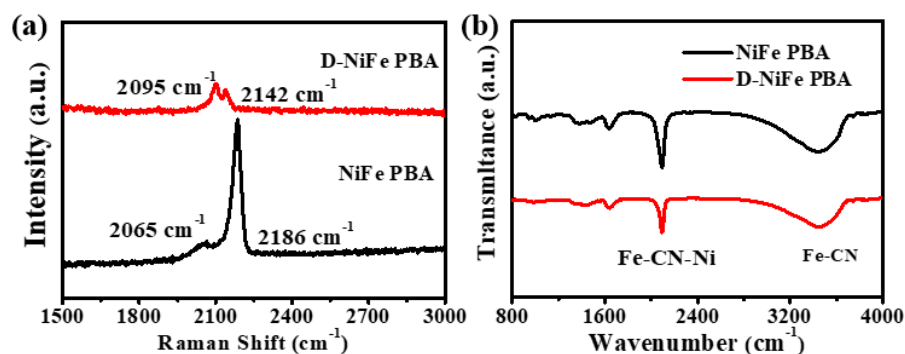
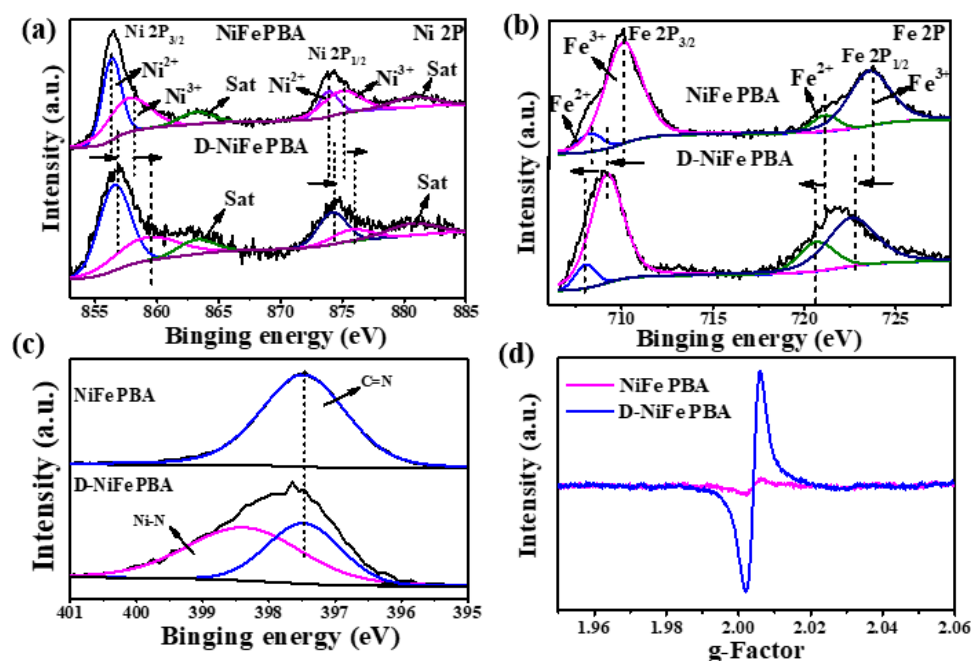


Figure 3. (a) FT-IR spectra (b) Ramam spectra of NiFe PBA and D-NiFe PBA.

The surface chemical states of the NiFe PBA and D-NiFe PBA were further investigated by XPS measurement. In the Ni  $2p_{3/2}$  XPS spectra (Figure 4a), the peaks at 859.5 and 856.3 eV were attributed to  $\text{Ni}^{3+}$  and  $\text{Ni}^{2+}$  in the NiFe PBA, respectively. Compared to the NiFe PBA, the peaks of the D-NiFe PBA were slightly shifted toward higher binding energies. Meanwhile, the peaks of  $\text{Fe}^{2+}$  at 708.2 eV and  $\text{Fe}^{3+}$  at 710.3 eV for Fe  $2p_{3/2}$  in the D-NiFe PBA shown in Figure 4b were shifted toward a lower binding energy than that of the NiFe PBA, indicating electron transfer between the Ni and Fe, which led to an increase in the Ni oxidation state [26,27]. The higher oxidation states of Ni in the D-NiFe PBA were more easily reconstructed during the OER via the formation of a NiFeOOH active layer, which led to the better OER activity of the D-NiFe PBA. In addition, the binding energy of the N 1s peaks (Figure 4c) located at 397.9 eV corresponded to the C=N in the NiFe PBA, which confirmed the formation of the PBA. However, the two de-convoluted peaks in the D-NiFe PBA corresponded to C=N (397.9 eV) and Ni-N (398.5 eV), which may be due to the formation of  $\text{V}_{\text{CN}}$  [28,29]. In addition, the O 1s XPS spectra of the NiFe PBA and D-NiFe PBA are shown in Figure S2. The peaks centered at the binding energies of 529.9, 531.44 and 533.05 eV were assigned to oxygen–metal bonds ( $\text{M} = \text{Ni}$  or  $\text{Fe}$ ), hydroxyl groups, and adsorbed molecular water molecules, respectively. The intensity of the M-O peak increased after the  $\text{NaBH}_4$  reduction, indicating the formation of surface M-O bonding that was induced by the  $\text{NaBH}_4$  reduction [30,31]. In order to demonstrate the generation of  $\text{V}_{\text{CN}}$  in the NiFe PBA after the  $\text{NaBH}_4$  reduction, electron paramagnetic resonance (EPR) spectrometry was employed. As shown in Figure 4d, the EPR signal mainly originated from the unpaired electrons of the  $\text{Ni}^{3+}$  ( $t_2g^6e_g^1$ ) species, suggesting that the generation of CN vacancies when increasing the oxidation state of Ni [32]. The D-NiFe PBA showed a symmetric signal at a magnetic field of  $g = 2.00$ , indicating the presence of  $\text{V}_{\text{CN}}$  in the lattice [14,33]. The EPR intensity of the D-NiFe PBA was much stronger than that of the NiFe PBA, which implied that the  $\text{NaBH}_4$  treatment generated a large amount of  $\text{V}_{\text{CN}}$ . This was consistent with reports in the literature [5,34].



**Figure 4.** (a) Ni 2p spectra, (b) Fe 2p XPS spectra, (c) N 1s spectra, and (d) EPR spectra of NiFe PBA and D-NiFe PBA.

The electrocatalytic activity of the D-NiFe PBA and NiFe PBA for the OER was assessed in a 1M KOH solution. As shown in Figure 5a, the onset potential of the D-NiFe PBA (1.51 V) was compared to that of the NiFe PBA (1.68 V) and IrO<sub>2</sub> (1.59 V). This indicated that the electrocatalytic performance of the D-NiFe PBA was significantly improved. The D-NiFe PBA showed oxidation peaks at around 1.4 V prior to the oxygen evolution, which were ascribed to the oxidation of Ni<sup>2+</sup> to Ni<sup>3+</sup>. To avoid the interference of the oxidation peaks of Ni<sup>2+</sup> to Ni<sup>3+</sup>, the overpotential at a current density of 10 mA cm<sup>-2</sup> was used as a benchmark for the comparison of the OER activity [30,31]. The Tafel plots of the samples are depicted in Figure 5b, and the Tafel slope of the D-NiFe PBA (67.92 mV dec<sup>-1</sup>) was much smaller than that of the NiFe PBA (141.94 mV dec<sup>-1</sup>) as well as most of the previously reported results (Table S2), indicating the high OER kinetics of the D-NiFe PBA. Furthermore, EIS was employed to obtain the  $R_{ct}$  values of the catalysts at a 280 mV overpotential, and the corresponding Nyquist plot is shown in Figure S3. Both the NiFe PBA and D-NiFe PBA presented two capacitive arcs over the entire frequency range of the Nyquist plot. Impressively, this revealed that the D-NiFe PBA had a lower charge transfer resistance than of NiFe PBA, indicating the better OER kinetics in the D-NiFe PBA.

To demonstrate the activity origin of the prepared catalyst, the ECSA was determined by measuring the capacitive current associated with double-layer charging from the scan-rate dependence of the CVs (Figure S4). The capacitance currents shown in Figure 5c were obtained from the corresponding CV curves. The  $C_{dl}$  of the D-NiFe PBA was calculated to be 11.26 mF cm<sup>-2</sup>, which was almost 28 times as high as that of the NiFe PBA (0.39 mF cm<sup>-2</sup>). This result suggested that the D-NiFe PBA exhibited a superior intrinsic activity [35]. Moreover, Figure 5d clearly shows that the D-NiFe PBA exhibited remarkable stability for over 100 h under an applied current density of 10 mA cm<sup>-2</sup>.

This excellent OER activity was closely dependent on the formation of  $V_{CN}$ .

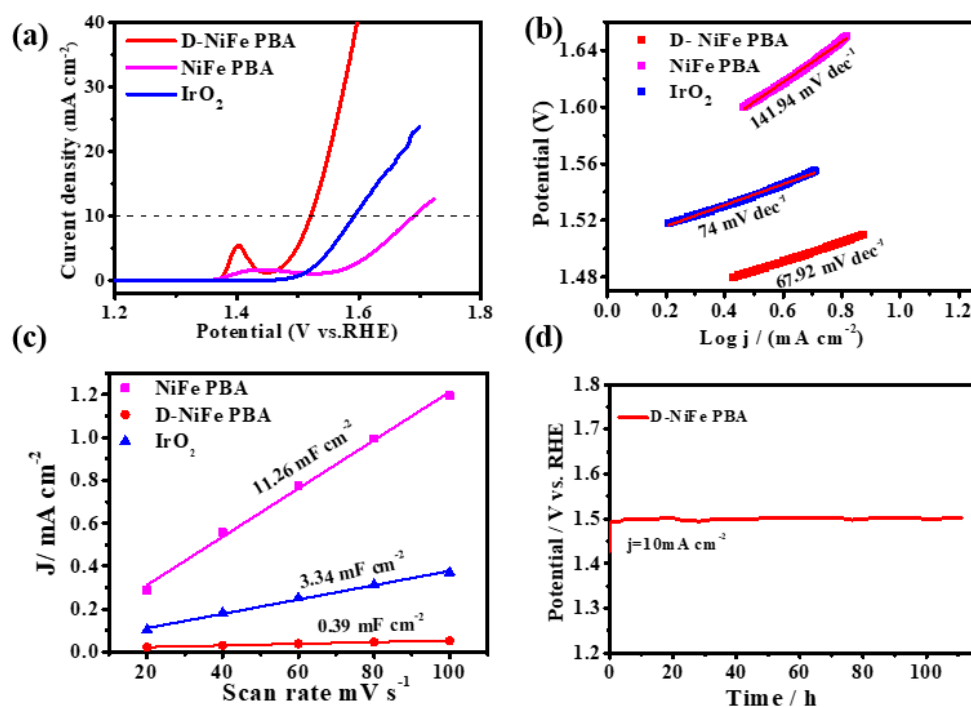


**Figure 5.** (a) LSV curves, (b) Tafel plot, (c) Cdl obtained from the data in CV curves recorded at different scanning rates for NiFe PBA, D-NiFe PBA and IrO<sub>2</sub>, (d) Current density as a function of scan rate for D-NiFe PBA.

Although a remarkably improved OER activity was achieved in the D-NiFe PBA, the D-NiFe PBA would undergo a transformation into the corresponding metal hydroxides phases during the OER process, which could function as an active catalytic species to proceed the OER. Therefore, a series of characterizations were carried out to investigate the cycled D-NiFe PBA. From the SEM findings before and after the 24 h OER cycling test shown in Figure S5, the D-NiFe PBA changed from thin nanosheets to thick nanosheets with obvious aggregation. The FT-IR spectrum was obtained, as shown in Figure S6, where the D-NiFe PBA exhibited three bands at 3650, 880, and 640 cm<sup>-1</sup> after 24 h of activation, which corresponded to O-H, Fe-OH, and Ni-OH bending, respectively. Meanwhile, the Fe-OH bond at 880 cm<sup>-1</sup> in the NiFe PBA was only detected in trace amounts after the 24 h OER test [3,13,36]. In addition, PXRD was also used to study the structural change of the products after the OER reaction (Figure S7). The results confirmed the formation of NiOOH and FeOOH in the D-NiFe PBA, as shown in Figure S5. However, FeOOH could not be found in the NiFe PBA. The reason was attributed to anion exchange between [Fe(CN)<sub>6</sub>]<sup>3-</sup> and OH<sup>-</sup> in the NiFe PBA during the OER, leading to Fe leaching and a rapid degradation of the catalytic activity, while Fe in the D-NiFe PBA could be incorporated into the active species to form Fe-OH bonds, and this phenomenon was also evidenced in a previous study [3,7]. In comparison, the excellent catalytic performance of the D-NiFe PBA was attributed to the much-more-exposed active sites from the rich CN vacancies and the formation of a NiFe oxygen (hydroxide) active surface layer during the OER. Apart from this, the energy-dispersive X-ray spectroscopy (EDX) results shown in Figure S8 showed that most of the iron species in the D-NiFe PBA was well retained after the 24 h OER reaction. In contrast, the NiFe PBA lost most of its Fe species after 24 h of continuous OER reaction. These results were in good agreement with the XRD and IF-IR results of the D-NiFe PBA after the 24 h OER reaction, indicating the excellent catalytic stability of the D-NiFe PBA in the OER.

#### 4. Conclusions

In conclusion, we successfully synthesized a D-NiFe PBA electrocatalyst with rich  $V_{CN}$  by a simple and convenient  $\text{NaBH}_4$  reduction approach. The  $V_{CN}$  not only modulated the local electronic structure and coordination environment of the Ni and Fe sites in the D-NiFe PBA but also enabled the D-NiFe PBA to produce highly active NiFe oxygen (hydroxide) species in the OER process that facilitated the OER. Compared with the initial NiFe PBA, the OER performance of the D-NiFe PBA was substantially enhanced (280 mV at  $10 \text{ mA cm}^{-2}$ ), and it had a superior stability over 100 h even in alkaline electrolytes. This reported approach promises to open the possibility of performance enhancement for other PBA electrocatalysts.

**Supplementary Materials:** The following supporting information can be downloaded at: <https://www.mdpi.com/article/10.3390/colloids7010014/s1>, Figure S1. (a) SEM images of NiFe PBA (b) TEM element mapping D-NiFe PBA of Ni, Fe, N, and C. Figure S2. O 1s spectra of NiFe PBA and D-NiFe PBA. Figure S3. Nyquist plots of NiFe PBA and D-NiFe PBA. Figure S4. CV curves of (a) D-NiFe PBA (b) NiFe PBA (c)  $\text{IrO}_2$ . Figure S5. SEM images of D-NiFe PBA before (a) and after (b) 24 h OER test. Figure S6. FT-IR spectra of NiFe PBA and D-NiFe PBA before and after 24 h OER test. Figure S7. XRD spectra of NiFe PBA and D-NiFe PBA after 24 h OER test. Figure S8. EDX spectra of NiFe PBA and D-NiFe PBA before and after 24 h OER test. Table S1. The atomic ratio obtained from ICP (measuring Fe and Ni) and elemental analysis (measuring C and N). Table S2. The comparison of OER activity of D-NiFe PBA with recently reported other nonnoble-metal OER catalysts under 1 M KOH. References [5,6,37–45] are cited in the Supplementary Materials.

**Author Contributions:** M.Z. wrote the manuscript draft and performed experiment and data analysis. X.G. and G.X. designed and guided the project and refined the manuscript. W.W. and Z.W. contributed to the experiment testing and result discussion. All authors have read and agreed to the published version of the manuscript.

**Funding:** This work was supported by the Key projects of intergovernmental international cooperation in key R&D programs of the Ministry of science and technology of China (No. 2021YFE0115800), the National Science Funding Committee of China (No. U20A20250, 21973074), and the Science and Technology Committee of Shaanxi Province (Grant No. 2020JZ-42).

**Data Availability Statement:** Data is contained within the article and supplementary material.

**Conflicts of Interest:** The authors declare no conflict of interest.

#### References

1. Singh, T.I.; Rajeshkhanna, G.; Pan, U.N.; Kshetri, T.; Lin, H.; Kim, N.H.; Lee, J.H. Alkaline Water Splitting Enhancement by MOF-Derived Fe-Co-Oxide/Co@NC-mNS Heterostructure: Boosting OER and HER through Defect Engineering and In Situ Oxidation. *Small* **2021**, *17*, 2101312. [CrossRef]
2. Asnavandi, M.; Yin, Y.; Li, Y.; Sun, C.; Zhao, C. Promoting Oxygen Evolution Reactions through Introduction of Oxygen Vacancies to Benchmark NiFe-OOH Catalysts. *ACS Energy Lett.* **2018**, *3*, 1515–1520. [CrossRef]
3. Jo, S.; Kwon, J.; Choi, S.; Lu, T.; Byeun, Y.; Han, H.; Song, T. Engineering  $[\text{Fe}(\text{CN})_6]^{3-}$  vacancy via free-chelating agents in Prussian blue analogues on reduced graphene oxide for efficient oxygen evolution reaction. *Appl. Surf. Sci.* **2022**, *574*, 151620. [CrossRef]
4. Jo, Y.; Cho, S.; Seo, J.; Ahmed, A.T.A.; Lee, C.H.; Seok, J.H.; Hou, B.; Patil, S.A.; Park, Y.; Shrestha, N.K.; et al. Experimental and Theoretical Insights into the Borohydride-Based Reduction-Induced Metal Interdiffusion in Fe-Oxide@NiCo<sub>2</sub>O<sub>4</sub> for Enhanced Oxygen Evolution. *ACS Appl. Mater. Interfaces* **2021**, *13*, 53725–53735. [CrossRef]
5. Nai, J.; Zhang, J.; Lou, X.W.D. Construction of single-crystalline Prussian blue analog hollow nanostructures with tailorable topologies. *Chem* **2018**, *4*, 1967–1982. [CrossRef]
6. Feng, Y.; Wang, X.; Dong, P.; Li, J.; Feng, L.; Huang, J.; Wang, C. Boosting the activity of Prussian-blue analogue as efficient electrocatalyst for water and urea oxidation. *Sci. Rep.* **2019**, *9*, 15965. [CrossRef]
7. Jiang, M.; Fan, X.; Cao, S.; Wang, Z.; Yang, Z.; Zhang, W. Thermally activated carbon–nitrogen vacancies in double-shelled NiFe Prussian blue analogue nanocages for enhanced electrocatalytic oxygen evolution. *J. Mater. Chem. A* **2021**, *9*, 12734–12745. [CrossRef]
8. Xuan, C.; Zhang, J.; Wang, J.; Wang, D. Rational design and engineering of nanomaterials derived from prussian blue and its analogs for electrochemical water splitting. *Chem. Asian J.* **2020**, *15*, 958–972. [CrossRef]
9. Wang, Y.; Kong, B.; Zhao, D.; Wang, H.; Selomulya, C. Strategies for developing transition metal phosphides as heterogeneous electrocatalysts for water splitting. *Nano Today* **2017**, *15*, 26–55. [CrossRef]

10. Li, W.J.; Han, C.; Cheng, G.; Chou, S.L.; Liu, H.K.; Dou, S.X. Chemical properties, structural properties, and energy storage applications of Prussian blue analogues. *Small* **2019**, *15*, 1900470. [[CrossRef](#)]
11. Zhou, W.-Y.; Sun, R.; Li, S.-S.; Guo, Y.; Shen, W.; Wang, J.; Deepak, F.L.; Li, Y.; Wang, Z. Engineering surface electron and active site at electrochemical sensing interface of CN vacancy-mediated Prussian blue analogue for analysis of heavy metal ions. *Appl. Surf. Sci.* **2021**, *564*, 150131. [[CrossRef](#)]
12. Hou, J.; Tang, Z.; Wei, K.; Lai, Q.; Liang, Y. Surface reconstruction of Ni doped Co-Fe Prussian blue analogues for enhanced oxygen evolution. *Catal. Sci. Technol.* **2021**, *11*, 1110–1115. [[CrossRef](#)]
13. Yu, Z.Y.; Duan, Y.; Liu, J.D.; Chen, Y.; Liu, X.K.; Liu, W.; Ma, T.; Li, Y.; Zheng, X.S.; Yao, T.; et al. Unconventional CN vacancies suppress iron-leaching in Prussian blue analogue pre-catalyst for boosted oxygen evolution catalysis. *Nat. Commun.* **2019**, *10*, 2799. [[CrossRef](#)]
14. Lai, C.; Li, H.; Sheng, Y.; Zhou, M.; Wang, W.; Gong, M.; Jiang, K. 3D Spatial Combination of CN Vacancy-Mediated NiFe-PBA with N-Doped Carbon Nanofibers Network toward Free-Standing Bifunctional Electrode for Zn-Air Batteries. *Adv. Sci.* **2022**, *9*, 2105925. [[CrossRef](#)]
15. Chi, H.; Liu, J.; Zhang, X.; Xue, X.; Zhang, D.; Lin, X.; Huang, P.; Sun, L.; Xiong, J.; Cai, P.; et al. Synergetic defects boost charge separation in CN for enhanced photocatalytic water splitting. *J. Mater. Chem. C* **2020**, *8*, 9366–9372. [[CrossRef](#)]
16. Xiang, K.; Wu, D.; Fan, Y.; You, W.; Zhang, D.; Luo, J.L.; Fu, X.Z. Enhancing bifunctional electrodes of oxygen vacancy abundant ZnCo<sub>2</sub>O<sub>4</sub> nanosheets for supercapacitor and oxygen evolution. *Chem. Eng. J.* **2021**, *425*, 130583. [[CrossRef](#)]
17. Yan, K.L.; Shang, X.; Liu, Z.Z.; Dong, B.; Lu, S.S.; Chi, J.Q.; Liu, C.G. A facile method for reduced CoFe<sub>2</sub>O<sub>4</sub> nanosheets with rich oxygen vacancies for efficient oxygen evolution reaction. *Int. J. Hydrogen Energy* **2017**, *42*, 24150–24158. [[CrossRef](#)]
18. Wang, X.; Li, T.T.; Zheng, Y.Q. Co<sub>3</sub>O<sub>4</sub> nanosheet arrays treated by defect engineering for enhanced electrocatalytic water oxidation. *Int. J. Hydrogen Energy* **2018**, *43*, 2009–2017. [[CrossRef](#)]
19. Chen, Z.; Fei, B.; Hou, M.; Yan, X.; Chen, M.; Qing, H.; Wu, R. Ultrathin Prussian blue analogue nanosheet arrays with open bimetal centers for efficient overall water splitting. *Nano Energy* **2020**, *68*, 104371. [[CrossRef](#)]
20. Zhang, X.; Khan, I.U.; Huo, S.; Zhao, Y.; Liang, B.; Li, K.; Wang, H. In-situ integration of nickel-iron Prussian blue analog heterostructure on Ni foam by chemical corrosion and partial conversion for oxygen evolution reaction. *Electrochim. Acta* **2020**, *363*, 137211. [[CrossRef](#)]
21. Zhang, C.; Chen, J.; Zhang, J.; Luo, Y.; Chen, Y.; Xue, Y.; Yan, Y.; Jiao, Y.; Wang, G.; Wang, R. The activation of inert NiFe Prussian Blue analogues to boost oxygen evolution reaction activity. *J. Colloid Interface Sci.* **2022**, *607*, 967–977. [[CrossRef](#)] [[PubMed](#)]
22. Zhang, W.; Zhao, Y.; Malgras, V.; Ji, Q.; Jiang, D.; Qi, R.; Hu, M. Synthesis of monocrystalline nanoframes of prussian blue analogues by controlled preferential etching. *Angew. Chem. Int. Ed.* **2016**, *55*, 8228–8234. [[CrossRef](#)] [[PubMed](#)]
23. Yang, H.; Liu, J.; Chen, Z.; Wang, R.; Fei, B.; Liu, H.; Guo, Y.; Wu, R. Unconventional bi-vacancies activating inert Prussian blue analogues nanocubes for efficient hydrogen evolution. *Chem. Eng. J.* **2021**, *420*, 127671. [[CrossRef](#)]
24. Wang, L.; Lu, Y.; Liu, J.; Xu, M.; Cheng, J.; Zhang, D.; Goodenough, J.B. A superior low-cost cathode for a Na-ion battery. *Angew. Chem. Int. Ed.* **2013**, *152*, 2018–2021. [[CrossRef](#)]
25. Risset, O.N.; Knowles, E.S.; Ma, S.; Meisel, M.W.; Talham, D.R. Rb<sub>i</sub>M<sub>k</sub>[Fe(CN)<sub>6</sub>]<sub>l</sub> (M = Co, Ni) Prussian Blue Analogue Hollow Nanocubes: A New Example of a Multilevel Pore System. *Chem. Mater.* **2012**, *25*, 42–47. [[CrossRef](#)]
26. Han, L.; Yu, X.Y.; Lou, X.W. Formation of Prussian-Blue-Analog Nanocages via a Direct Etching Method and their Conversion into Ni-Co-Mixed Oxide for Enhanced Oxygen Evolution. *Adv. Mater.* **2016**, *28*, 4601–4605. [[CrossRef](#)]
27. Xu, X.; Wang, T.; Su, L.; Zhang, Y.; Dong, L.; Miao, X. In Situ Synthesis of Superhydrophilic Amorphous NiFe Prussian Blue Analogues for the Oxygen Evolution Reaction at a High Current Density. *ACS Sustain. Chem. Eng.* **2021**, *9*, 5693–5704. [[CrossRef](#)]
28. Zhang, L.; Ma, Y.T.; Duan, J.J.; Yao, Y.Q.; Feng, J.J.; Wang, A.J. In-Situ construction of 3D hetero-structured sulfur-doped nanoflower-like FeNi LDH decorated with NiCo Prussian blue analogue cubes as efficient electrocatalysts for boosting oxygen evolution reaction. *J. Colloid Interface Sci.* **2022**, *611*, 205–214. [[CrossRef](#)]
29. Gao, Z.; Li, Y.; Zhang, C.; Zhang, S.; Jia, Y.; Dong, Y. An enzyme-free immunosensor for sensitive determination of procalcitonin using NiFe PBA nanocubes@ TB as the sensing matrix. *Anal. Chim. Acta* **2020**, *1097*, 169–175. [[CrossRef](#)]
30. Yi, X.; He, X.; Yin, F.; Chen, B.; Li, G.; Yin, H. Amorphous Ni-Fe-Se hollow nanospheres electrodeposited on nickel foam as a highly active and bifunctional catalyst for alkaline water splitting. *Dalton Trans.* **2020**, *20*, 6764–6775. [[CrossRef](#)]
31. Patil, S.J.; Chodankar, N.R.; Hwang, S.K.; Rama Raju, G.S.; Huh, Y.S.; Han, Y.K. Fluorine Engineered Self-Supported Ultrathin 2D Nickel Hydroxide Nanosheets as Highly Robust and Stable Bifunctional Electrocatalysts for Oxygen Evolution and Urea Oxidation Reactions. *Small* **2022**, *7*, 2103326. [[CrossRef](#)] [[PubMed](#)]
32. Zhao, Y.; Jia, X.; Chen, G.; Shang, L.; Waterhouse, G.I.; Wu, L.Z.; Zhang, T. Ultrafine NiO nanosheets stabilized by TiO<sub>2</sub> from monolayer NiTi-LDH precursors: An active water oxidation electrocatalyst. *J. Am. Chem. Soc.* **2016**, *20*, 6517–6524. [[CrossRef](#)] [[PubMed](#)]
33. Kim, M.; Park, J.H.; Lim, J.M.; Kim, H.; Kim, S. Conventional and photoinduced radioactive <sup>137</sup>Cs removal by adsorption on FeFe, CoFe, and NiFe Prussian blue analogues. *Chem. Eng. J.* **2021**, *405*, 126568. [[CrossRef](#)]
34. An, L.; Feng, J.; Zhang, Y.; Zhao, Y.; Si, R.; Wang, G.; Cheng, F.; Xi, P.; Sun, S. Controllable tuning of Fe-N nanosheets by Co substitution for enhanced oxygen evolution reaction. *Nano Energy* **2019**, *57*, 644–652. [[CrossRef](#)]
35. Feng, Y.; Wang, S.; Wang, H.; Zhong, Y.; Hu, Y. An efficient and stable Ni-Fe selenides/nitrogen-doped carbon nanotubes in situ-derived electrocatalyst for oxygen evolution reaction. *J. Mater. Sci.* **2020**, *55*, 13927–13937. [[CrossRef](#)]

36. Tian, X.; Cheng, C.; Qian, L.; Zheng, B.; Yuan, H.; Xie, S.; Choi, M.M. Microwave-assisted non-aqueous homogenous precipitation of nanoball-like mesoporous  $\alpha$ -Ni(OH)<sub>2</sub> as a precursor for NiO<sub>x</sub> and its application as a pseudocapacitor. *J. Mater. Chem. A* **2012**, *22*, 8029–8035. [[CrossRef](#)]
37. Kang, Y.; Wang, S.; Hui, K.; Li, H.-F.; Liang, F.; Wu, X.-L.; Zhang, Q.; Zhou, W.; Chen, L.; Chen, F.J. [Fe(CN)<sub>6</sub>] vacancy-boosting oxygen evolution activity of Co-based Prussian blue analogues for hybrid sodium-air battery. *Mater. Today Energy* **2021**, *20*, 100572.
38. Pan, Y.; Zhang, J.; Zhao, Z.; Shi, L.; Wu, B.; Zeng, L. Iron-doped metal-organic framework with enhanced oxygen evolution reaction activity for overall water splitting. *Int. J. Hydrogen Energy* **2021**, *46*, 34565–34573. [[CrossRef](#)]
39. Zhang, H.; Li, P.; Chen, S.; Xie, F.; Riley, D.J. Anodic Transformation of a Core-Shell Prussian Blue Analogue to a Bifunctional Electrocatalyst for Water Splitting. *Adv. Funct. Mater.* **2021**, *31*, 2106835. [[CrossRef](#)]
40. Zou, H.; Liu, X.; Wang, K.; Duan, Y.; Wang, C.; Zhang, B.; Zhou, K.; Yu, D.; Gan, L.-Y.; Zhou, X. Constructing highly active Co sites in Prussian blue analogues for boosting electrocatalytic water oxidation. *Chem. Commun.* **2021**, *57*, 8011–8014. [[CrossRef](#)]
41. Sun, W.; Wei, Z.; Qi, J.; Kang, L.; Li, J.; Xie, J.; Tang, B.; Xie, Y. Rapid and Scalable Synthesis of Prussian Blue Analogue Nanocubes for Electrocatalytic Water Oxidation. *Chin. J. Chem.* **2021**, *39*, 2347–2353. [[CrossRef](#)]
42. Jia, X.; Zhao, Y.; Chen, G.; Shang, L.; Shi, R.; Kang, X.; Zhang, T. Ni<sub>3</sub>FeN nanoparticles derived from ultrathin NiFe-layered double hydroxide nanosheets: An efficient overall water splitting electrocatalyst. *Adv. Energy Mater.* **2016**, *6*, 1502585. [[CrossRef](#)]
43. Karkera, G.; Sarkar, T.; Bharadwaj, M.D.; Prakash, A.S. Design and development of efficient bifunctional catalysts by tuning the electronic properties of cobalt-manganese tungstate for oxygen reduction and evolution reactions. *ChemCatChem* **2017**, *9*, 3681–3690. [[CrossRef](#)]
44. Li, M.; Xiong, Y.; Liu, X.; Bo, X.; Zhang, Y.; Han, C.; Guo, L. Facile synthesis of electrospun MFe<sub>2</sub>O<sub>4</sub> (M=Co, Ni, Cu, Mn) spinel nanofibers with excellent electrocatalytic properties for oxygen evolution and hydrogen peroxide reduction. *Nanoscale* **2015**, *7*, 8920–8930. [[CrossRef](#)]
45. Yang, Y.; Lin, Z.; Gao, S.; Su, J.; Lun, Z.; Xia, G.; Chen, Q. Tuning electronic structures of nonprecious ternary alloys encapsulated in graphene layers for optimizing overall water splitting activity. *ACS Catal.* **2017**, *7*, 469–479. [[CrossRef](#)]

**Disclaimer/Publisher's Note:** The statements, opinions and data contained in all publications are solely those of the individual author(s) and contributor(s) and not of MDPI and/or the editor(s). MDPI and/or the editor(s) disclaim responsibility for any injury to people or property resulting from any ideas, methods, instructions or products referred to in the content.